Author/s:
Zheng, F;Angmo, D;Hall, CR;Rubanov, S;Yuan, F;Laird, JS;Gao, M;Smith, TA;Ghiggino, KP

Title:
Brownian Tree-Shaped Dendrites in Quasi-2D Perovskite Films and Their Impact on Photovoltaic Performance

Date:
2022-05-01

Citation:
Zheng, F., Angmo, D., Hall, C. R., Rubanov, S., Yuan, F., Laird, J. S., Gao, M., Smith, T. A. & Ghiggino, K. P. (2022). Brownian Tree-Shaped Dendrites in Quasi-2D Perovskite Films and Their Impact on Photovoltaic Performance. Advanced Materials Interfaces, 9 (13), https://doi.org/10.1002/admi.202102231.

Persistent Link:
https://hdl.handle.net/11343/308129

ADVANCED MATERIALS INTERFACES
www.advmatinterfaces.de

Brownian Tree-Shaped Dendrites in Quasi-2D Perovskite Films and Their Impact on Photovoltaic Performance

*Fei Zheng, Dechan Angmo, Christopher R. Hall, Sergey Rubanov, Fangfang Yuan, Jamie S. Laird, Mei Gao, Trevor A. Smith, and Kenneth P. Ghiggino**

Quasi-2D Ruddlesden–Popper perovskites (RPPs) are candidates for constructing perovskite solar cells (PSCs) with superior stability due to their tolerance to the external environment. Fully understanding the film growth mechanism and structure is crucial to further improve the performance of 2D-PSCs while maintaining device stability. In this work, the origin of Brownian tree-shaped dendrites formed in hot-cast methylammonium chloride (MACl)-doped $BA_2MA_{n-1}Pb_nI_{3n+1}$ ($<n> = 5$) quasi-2D perovskite films are reported. Investigations based on optical, electronic, atomic force, and fluorescence microscopies reveal that the dendrites are assembled from large-*n* RPPs-dominated grains, while the nondendritic film area is composed of small-*n* RPPs grains and associated with film surface pits caused by the evaporation of MACl. It is proposed that these dendrites are grown by the diffusion-limited aggregation of the MA-rich intermediate phase domains that initially crystallize from the precursor. The formation of these dendrites in quasi-2D perovskite films upon MACl doping is accompanied by improved organization and crystallinity of the 2D RPPs, which benefits the photovoltaic performance. This work provides new insights into the formation mechanism of quasi-2D perovskite films that should assist device engineering strategies to further improve the performance of 2D PSCs.

1. Introduction

The recent development of Ruddlesden–Popper phase quasi-2D perovskites has attracted growing attention owing to their improved stability compared to conventional 3D organic–inorganic lead halide perovskites.[1] Ruddlesden–Popper perovskites (RPPs), labeled as $R_2A_{n-1}Pb_nX_{3n+1}$ (X = Br, I), are formed by incorporating long-alkyl-chain ammonium cations (R^+) into the 3D $APbX_3$ perovskite framework through the stoichiometric design of the precursor solution.[2] A^+ cations are the commonly used short-chain organic methylammonium (MA^+) and formamidinium (FA^+) cations, while R^+ has been expanded to a wide spectrum, typically *n*-butylammonium (BA^+), phenethylammonium (PEA^+), 2-thiophenemethylammonium ($ThMA^+$).[3] Quasi-2D RPPs slabs characterized by *n* layers of corner-sharing [$APbX_6$] octahedral sheets sandwiched by two layers of R^+ spacer ligands can be assembled to single crystals or polycrystalline films by van der Waals forces. Compared to 3D perovskites, the hydrophobicity and low permittivity of R^+ ligands give RPPs greater resistance to moisture, oxygen, and UV light, as well as suppressed ion migration, which addresses many of the instability issues faced by perovskite solar cells (PSCs).[4] The dielectric and quantum confinement brought by the R^+ ligands make RPPs behave like quantum wells, where the bandgap can be tuned by changing *n* values.[5] These intriguing properties with both chemical and quantum-mechanical tunability have led to the extensive exploration of RPPs not only for fundamental research but also for applications in high-performance photodetectors, light-emitting diodes, and PSCs.[6]

Owing to the insulating nature of typical R^+ ligands, charge carrier movement in individual quasi-2D RPPs slabs is mainly constrained along the slab plane and inter-slab charge transfer perpendicular to the 2D-plane is inhibited.[7] The universal approach toward quasi-2D RPPs PSCs with high power conversion efficiency (PCE) relies on the alignment of RPPs slabs perpendicular to the substrate within perovskite films to ensure efficient charge transport and extraction by top and bottom surface contacts. However, the presence of multiphase RPPs consisting of slabs with thickness (*n*) deviating from the nominal value <*n*> inevitably complicates the energy landscape within the quasi-2D perovskite

F. Zheng, C. R. Hall, F. Yuan, J. S. Laird, T. A. Smith, K. P. Ghiggino
School of Chemistry and ARC Centre of Excellence in Exciton Science
The University of Melbourne
Parkville, Victoria 3010, Australia
E-mail: ghiggino@unimelb.edu.au
D. Angmo, M. Gao
Devices and Engineered Systems Program
CSIRO Manufacturing
Clayton, VIC 3168, Australia
S. Rubanov
Ian Holmes Imaging Centre
Bio21 Institute
The University of Melbourne
Victoria 3010, Australia
The ORCID identification number(s) for the author(s) of this article can be found under https://doi.org/10.1002/admi.202102231.

DOI: 10.1002/admi.202102231

films, challenging the rational design of device structures for high-performance PSCs. Since the early success of BA-based quasi-2D PSCs with a PCE of 12.5%,[1b] substantial efforts have been made to tune the phase distribution and spatial orientation of RPPs slabs within the quasi-2D perovskite films into the optimized configuration, boosting the highest PCE reported to 19.06%.[3d] The methods adopted include compositional design by tailoring the spacer R^+ cations,[8] solvent engineering by using dimethylformamide (DMF)/dimethyl sulfoxide solvent mixtures,[9] and incorporating volatile salt additives, such as NH_4Cl, MACl, NH_4SCN, etc.[3a,10] The majority of quasi-2D perovskite films for high-PCE PSCs has been described by a sequential distribution model, wherein small-*n* (thin) RPPs are located in the bottom and large-*n* (thick) RPPs on the top of quasi-2D perovskite films.[11] Recently, we found evidence for a sandwich-like phase distribution model, featuring a large-*n*/small-*n*/large-*n* RPPs stacking configuration in the direction perpendicular to the substrate plane, to describe the structure of quasi-2D perovskite films prepared on hot substrates.[12] The resulting fusiform-like bandgap facilitates excitons funneling from the film interior to both surfaces for dissociation to ensure efficient charge collection by the electrodes.[12]

Despite the extensive reports of the microstructure of quasi-2D RPPs films, the macroscale evaluation of the film quality and phase distribution in the lateral direction, which is more relevant to revealing the film formation kinetics, have largely been ignored.[13] To fully understand the crystallization mechanisms in quasi-2D RPPs films, and consolidate the principles for improving the performance of 2D PSCs based on the control of fabrication conditions, further work is required to reveal the morphology of quasi-2D perovskite films at an extended spatial scale. Hundreds of micrometer-sized clusters exhibiting radial dendrites have been widely reported in 3D perovskite films prepared with fast thermal annealing, such as the flash infrared annealing method and slot-die coating.[14] These features, caused by highly oriented or faced crystal growth from the nucleation sites, lead to fewer nonradiative defects and improved optoelectronic properties of 3D perovskites.[14b] However, to our knowledge, whether quasi-2D perovskite films exhibit the same crystallization and film growth mechanism as the 3D perovskites and have similar dendritic patterns or not has not been revealed to date.

In this work, dendrites with the shape of a Brownian tree formed in the MACl-doped $BA_2MA_{n-1}Pb_nI_{3n+1}$ ($\langle n\rangle = 5$) quasi-2D perovskite films prepared by the hot-casting method are demonstrated and systematically investigated for the first time. Scanning electron microscopy (SEM) and atomic force microscopy (AFM) measurements reveal the existence of indentations (or pits) spreading over the surface of the nondendrite areas of the film. The compositional difference between the dendritic and nondendritic regions is identified by scanning transmission electron microscopy (STEM) and steady-state/time-resolved photoluminescence (TRPL) spectroscopies, indicating more large-*n* RPPs appear in the dendrites while small-*n* RPPs dominate the film composition underneath the pits. We propose that the Brownian tree-shaped dendrites in quasi-2D perovskite films are formed by diffusion-limited aggregation of the MA-rich intermediate phase domains. Grazing incidence wide-angle X-ray scattering (GIWAXS) and transient absorption (TA) studies combined with the performance characterization of the constructed 2D PSCs revealed that the formation of these dendrites in quasi-2D perovskite films upon MACl doping is accompanied by improved organization and crystallinity of the component 2D RPPs, thus substantially benefitting the photovoltaic performance of 2D PSCs. Aging the MACl-doped quasi-2D perovskite films led to the compositional and structural refinement desirable for the optimized performance of 2D PSCs. This work provides new insight into the formation mechanism of quasi-2D perovskite films and has significant implications for the controlled fabrication of high-performance optoelectronic devices based on quasi-2D perovskite films.

2. Results and Discussion

Our previous studies have demonstrated that the PCE and operational stability of 2D PSCs based on the hot-drop-cast $BA_2MA_{n-1}Pb_nI_{3n+1}$ ($\langle n\rangle = 5$) quasi-2D perovskite films can be significantly enhanced by doping with methylammonium chloride (MACl, 6 mol%).[15] **Figure 1**a,b shows the optical transmission microscopic images of $BA_2MA_{n-1}Pb_nI_{3n+1}$ ($\langle n\rangle = 5$) quasi-2D perovskite films without and with MACl doping. The film prepared without MACl doping is homogenous in transmission and almost free of any anisotropic patterns. By contrast, MACl doping leads to the formation of dendrites with lateral dimensions of ≈200 μm and lower visible light transmittance (dark regions) evenly distributed across the quasi-2D perovskite film. Similar dendritic patterns also appear in the MACl-doped $BA_2MA_{n-1}Pb_nI_{3n+1}$ ($\langle n\rangle = 5$) quasi-2D perovskite films prepared by the hot-spin-coating method and f-$PEA_2MA_{n-1}Pb_nI_{3n+1}$ ($\langle n\rangle = 5$) films (Figure S1a,b, Supporting Information), indicating the patterns caused by MACl doping of quasi-2D perovskite films are common, irrespective of the type of spacer cations (R^+) and film preparation method. These randomly branched dendrites formed in quasi-2D perovskite films substantially differ from the radial dendrites (clusters) observed in the 3D $MAPbI_3$ cast on the temperature elevated substrate (Figure S2, Supporting Information), suggesting crystallization in quasi-2D perovskite and 3D perovskite films involves different pathways. In addition, as shown in Figure S3a,b in the Supporting Information, the dendrites in MACl-doped $BA_2MA_{n-1}Pb_nI_{3n+1}$ films have a smaller size for the $\langle n\rangle = 2$ samples (BA/MA = 2:1) compared to the $\langle n\rangle = 5$ samples (BA/MA = 1:2), and disappear in the $\langle n\rangle = 1$ pure 2D films (BA/MA = 1:0), indicating the Brownian tree-shaped dendrites formed in quasi-2D perovskite films require the presence of MA cations.

Interestingly, the dendrites present in the MACl-doped $BA_2MA_{n-1}Pb_nI_{3n+1}$ ($\langle n\rangle = 5$) quasi-2D perovskite films are quite analogous to the Brownian trees formed through the diffusion-limited-aggregation (DLA) process, which arise in many types of multifractal phenomena such as electrodeposition, dielectric breakdown, and dendritic solidification.[16] The DLA model describes random aggregates of free particles undergoing Brownian motion that adhere to a seed point at the center and grow outward to form a cluster. The number of particles (N) scales with the cluster size (radius R) following Equation (1)[16a]

$$N \sim R^D = R^{d-A} \tag{1}$$

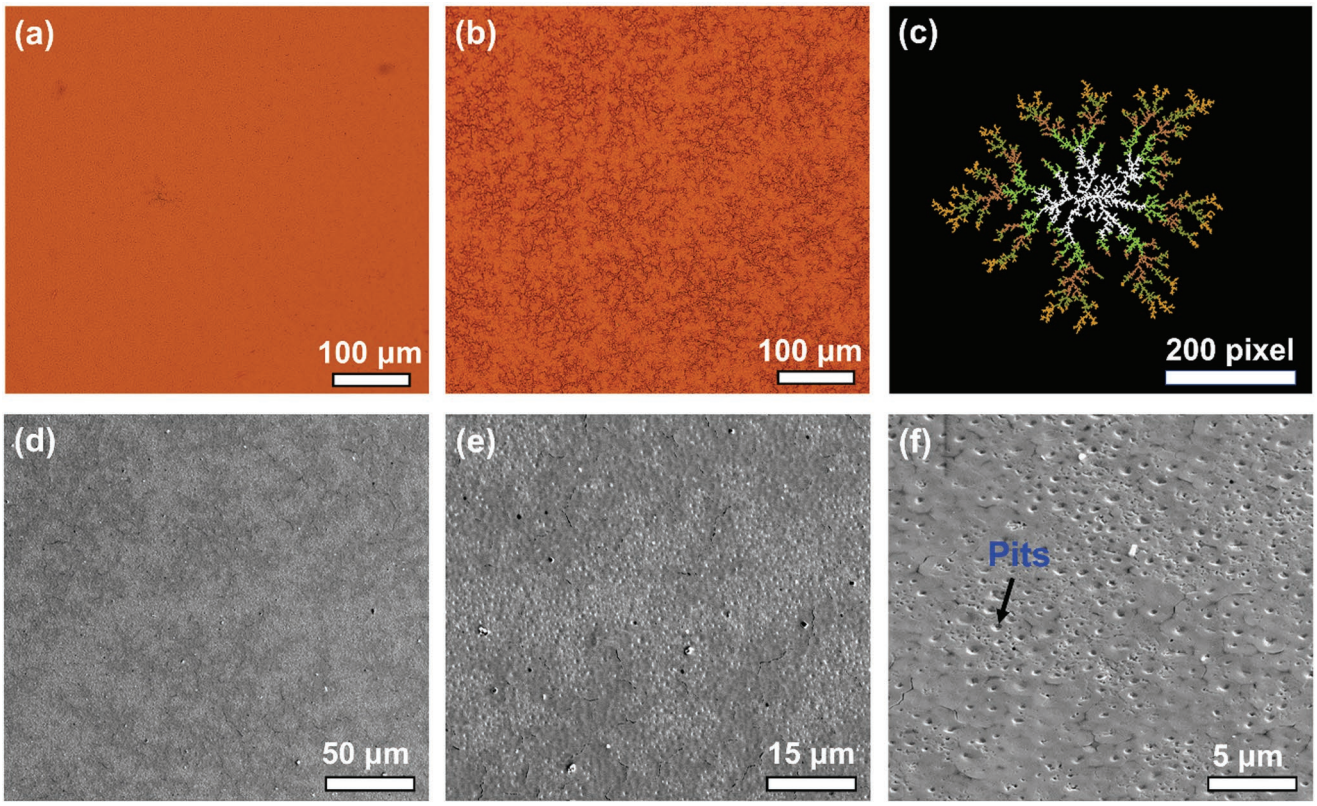

Figure 1. Optical transmission images of hot-drop-cast $BA_2MA_{n-1}Pb_nI_{3n+1}$ ($<n> = 5$) quasi-2D perovskite films prepared a) without and b) with MACl doping. c) A DLA-induced Brownian tree generated by computer simulation. d–f) SEM images of $BA_2MA_{n-1}Pb_nI_{3n+1}$ ($<n> = 5$) quasi-2D perovskite films obtained using various magnifications and tilt angles of d,e) 10° and f) 52°.

wherein D represents the Hausdorff dimension and d is the fractal dimension. Figure 1c depicts a Brownian tree generated from the DLA of 10 000 abstract round particles (size ~ 3 pixels) distributed in a 2D plane (644 × 644 pixels) based on an open-source computer simulation.[17] The ratio between the lateral size of the Brownian tree and the diameter of the composing elements is around 130. This simulated Brownian tree matches well in appearance to the dendrites shown in Figure 1b. Thus, we presume that the Brownian tree-shaped dendrites formed in the quasi-2D perovskite films are associated with a DLA process occurring during the film growth. As these dendrites accompany the performance enhancement of the 2D PSCs upon MACl doping, a detailed investigation was pursued to better understand the quasi-2D perovskite film formation mechanism and the film structure that ultimately governs charge-carrier dynamics and device performance.

SEM images of the front surface (film/air side) of the hot-drop-cast MACl-doped $BA_2MA_{n-1}Pb_nI_{3n+1}$ ($<n> = 5$) quasi-2D perovskite films with different magnification are shown in Figure 1d–f. Under low magnification (Figure 1d), the SEM image gives a similar contrast pattern to that of the optical transmission image, featuring ≈200 μm-sized dendrites that are darker compared to the background. Thus, it can be inferred that the dendrites observed in the optical image possessing low visible light transmittance correspond to film areas with low electron reflectance. As SEM images in this work were generated by collecting secondary electrons (SEs), a film topography with more edges and sharp points would lead to brighter images. An SEM image of the same film position at higher magnification (Figure 1e) illustrates that the surface of dendrites is smoother than the nondendritic background, within which many bright spots are apparent. By further increasing the magnification and tilting the film sample from 10° to 52°, the SEM image in Figure 1f shows that the bright spots in the nondendritic film areas are in fact depressions (or pits) in the surface, while dendritic regions are mostly free of pits. Thus, the film areas with a smooth surface (no pits) are strongly correlated with the Brownian tree-shaped dendrites formed in the quasi-2D perovskite films with MACl doping. However, no pits were found in the SEM image of the hot-cast $BA_2MA_{n-1}Pb_nI_{3n+1}$ ($<n> = 5$) quasi-2D perovskite films without MACl doping (Figure S4, Supporting Information), where dendrites were largely absent. This contrasts with the observation of pits in dendrite-free regions in MACl-doped films (Figure 1e). To better understand the origin of these differences, we explore the structure and composition of MACl-doped films.

The morphology of the hot-drop-cast MACl-doped $BA_2MA_{n-1}Pb_nI_{3n+1}$ ($<n> = 5$) quasi-2D perovskite films containing both dendritic and nondendritic areas was further explored with AFM. **Figure 2**a shows an AFM image recorded at the boundary between dendritic and nondendritic regions. Well-defined grain boundaries are observed, with both regions showing grains with lateral sizes of ≈1–2 μm. The ratio between the lateral size of the dendrites and the grain size can be

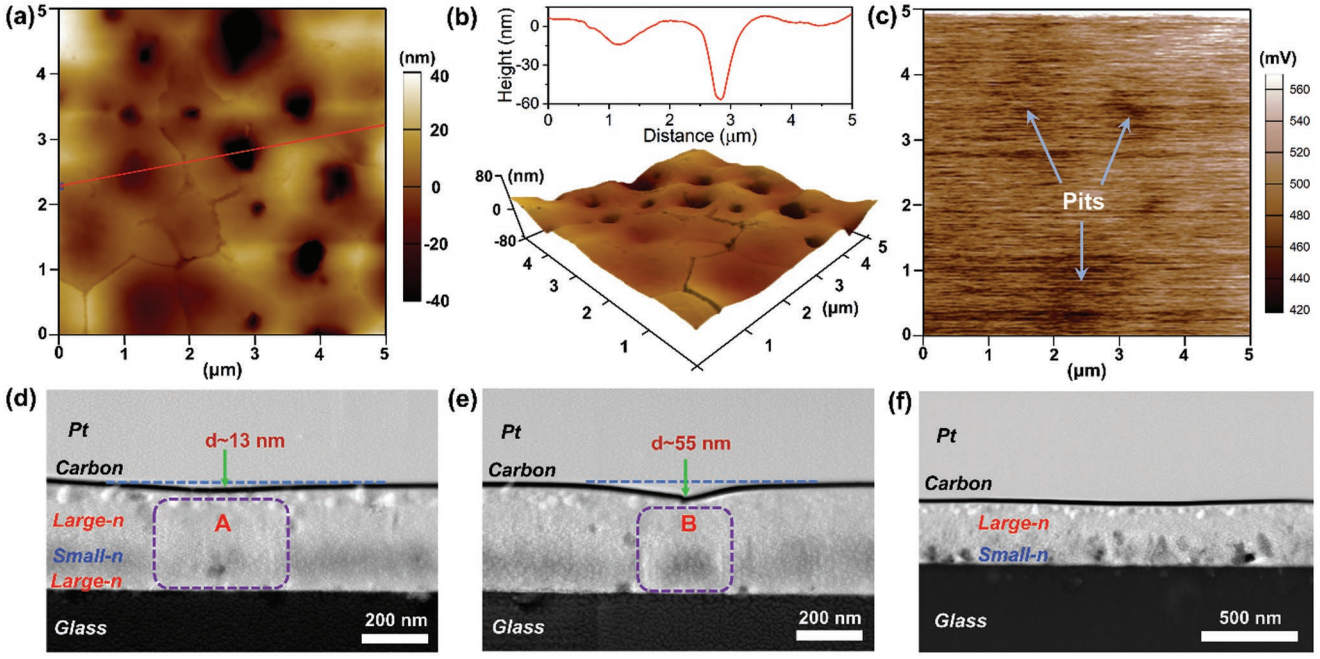

Figure 2. a) AFM 2D morphology of the MACl-doped $BA_2MA_{n-1}Pb_nI_{3n+1}$ (<n> = 5) quasi-2D perovskite films. b) The corresponding 3D topographic image (lower panel) and the height profile along the red labeled line shown in (a); c) KPFM image of the MACl-doped $BA_2MA_{n-1}Pb_nI_{3n+1}$ (<n> = 5) quasi-2D perovskite films. The HAADF STEM images of the MACl-doped $BA_2MA_{n-1}Pb_nI_{3n+1}$ (<n> = 5) quasi-2D perovskite cross-sectional film lamella from d) the dendritic film area (without pits) and e) the nondendritic film area (with pits); f) HAADF STEM image of $BA_2MA_{n-1}Pb_nI_{3n+1}$ (<n> = 5) quasi-2D perovskite films without MACl doping.

estimated as between 100 and 200, which is in agreement with that of the simulated Brownian tree (130). In contrast to 3D perovskite films, wherein the grain center has a higher altitude than the grain boundary,[18] the height of quasi-2D perovskite grains reduces from the boundaries toward the center. The height profile along the labeled line in Figure 2a, indicated in the upper panel of Figure 2b, shows the formation of deep pits in the nondendritic areas with depth ≈60 nm, as well as much shallower concavity in the dendritic region, with a depth of ≈10 nm. The 3D topography presented in the lower panel of Figure 2b offers a more intuitive demonstration of the distribution of pits over the quasi-2D perovskite films, further highlighting the existence of pits as revealed by the SEM images. It can be inferred that the smaller average film thickness for the nondendritic film areas (where pits occur) should be one of the reasons for the higher visible light transmittance observed in these regions compared to the dendrites (dark patterns in Figure 1a). Kelvin probe force microscopy (KPFM) characterization of this quasi-2D perovskite film was carried out to determine the local surface potential by tracking the contact potential differences (CPDs) between the tip and sample surface associated with the work function.[18] Figure 2c shows the distribution of CPD values over the film areas without and with pits. By comparison with the corresponding AFM 2D morphology shown in Figure S5 in the Supporting Information, 2D perovskite grains with pits possess a lower surface potential or work function compared to the flat grains without pits. As the Fermi-level of quasi-2D RPPs increases with the slab thickness (n),[19] the KPFM data are consistent with a higher density of small-n RPPs in the pits area than the dendritic area.

To identify the compositional difference between the dendrites and the nondendritic region, STEM characterization was applied to obtain the cross-sectional information for the $BA_2MA_{n-1}Pb_nI_{3n+1}$ (<n> = 5) quasi-2D perovskite film. A thin lamella sample of glass/quasi-2D perovskite/carbon/Pt (thickness ≈100 nm) was prepared by the lift-off FIB (focused ion beam) technique, as detailed in the Experimental Section.[20] The high-angle annular dark-field (HAADF) STEM images of perovskite lamella areas without and with pits are shown in Figure 2d,e, depicting each layer by distinct brightness contrast. As the intensity of the STEM image (Z-contrast) scales with the average atomic number (Z),[21] the dark and bright regions within the quasi-2D perovskite layer can be assigned to small-n RPPs (smaller Z) and large-n RPPs (larger Z) components, respectively.[12,22] Thus, a sandwich-like phase distribution reported by us previously,[12] comprising large-n/small-n/large-n regions along the vertical direction, applies to both film regions without pits (dendritic area) and with pits (nondendritic area). The estimated depth of shallow concave (≈13 nm) and deep pits (≈55 nm) is consistent with the AFM height profile, confirming the lamella in Figure 2d,e has been cut from the dendritic and nondendritic (pits) area of the quasi-2D perovskite film crossing the grain centers. The compositional difference between the two lamella areas is reflected in the phase distribution profiles around the grain centers, as labeled by rectangles A and B, respectively. Region-A of quasi-2D perovskite appears brighter compared to the neighboring sites of the film, suggesting more large-n (larger average thickness n) RPPs are concentrated in the center of the quasi-2D perovskite grains forming the dendrites. On the contrary, the

grain center underneath the pits (region-B) is dominated by the small-*n* RPPs components (darker). Based on these results, we propose that the evaporation of volatile MACl molecules leads to a local shortage of MA^+ cations and thus the formation of pits regions composed of a higher yield of small-*n* RPPs. By comparison, the HAADF STEM image of the $BA_2MA_{n-1}Pb_nI_{3n+1}$ ($\langle n \rangle = 5$) quasi-2D perovskite film without MACl doping is free of any pits (Figure 2f), giving a much flatter front surface than that of MACl-doped films. The HAADF STEM image shows an unorganized alignment of 2D RPPs within the film, with large-*n* RPPs allocated in the front (air) side and small-*n* RPPs randomly distributed on the bottom side. Thus, the evaporation of MACl during film formation also seems to play a key role in the assembly of well-aligned 2D RPPs within quasi-2D perovskite films required for high-performance 2D PSCs. Furthermore, the STEM images indicate that the component ratio of small-*n* to large-*n* RPPs for MACl-doped $BA_2MA_{n-1}Pb_nI_{3n+1}$ ($\langle n \rangle = 5$) film (Figure 2d,e) is larger than the un-doped film, which is consistent with our previous finding that MACl doping facilitates the formation of small-*n* RPPs.[15]

The lateral heterogeneity in the composition and the related photophysical properties of the MACl-doped $BA_2MA_{n-1}Pb_nI_{3n+1}$ ($\langle n \rangle = 5$) quasi-2D perovskite films were investigated by TR fluorescence microscopy. Images of the integrated PL intensity and the corresponding average PL lifetime of the quasi-2D perovskite film, generated by scanning a pulsed laser (420 nm) over the same film area, are presented in **Figure 3**a,b. Dendrites observed by the optical transmission imaging, SEM, and AFM can be recognized in the PL intensity image, showing much higher emission intensity compared to the nondendritic film area (see Figure 1a,b, in which darker regions correspond to higher absorbance and hence higher emission intensity). The PL average lifetime image is based on a triple-exponential decay function (Equation (2-a)) fit to each *x*–*y* position, from which an amplitude weighted average lifetime τ_m is calculated (Equation (2-b))[23]

$$I_{PL}(t) = A_1 \exp\left(-\frac{t}{\tau_1}\right) + A_2 \exp\left(-\frac{t}{\tau_2}\right) + A_3 \exp\left(-\frac{t}{\tau_3}\right) \quad (2\text{-a})$$

$$\tau_m = \left(\sum_{i=1}^{3} A_i \cdot \tau_i\right) \Big/ \left(\sum_{i=1}^{3} A_i\right) \quad (2\text{-b})$$

wherein $I_{PL}(t)$ is the time-dependent fluorescence intensity after photoexcitation, τ_i, A_i ($i = 1, 2, 3$) are the fitted decay time constants and the corresponding amplitudes. The average lifetime (τ_m) images show that the dendrites exhibit longer-lived emission than those in the nondendritic area containing pits. These results suggest that the dendritic and nondendritic regions feature significantly different intrinsic optoelectronic properties. The steady-state PL spectra collected from the dendritic region (point-A labeled) and nondendritic region (point-B) are shown

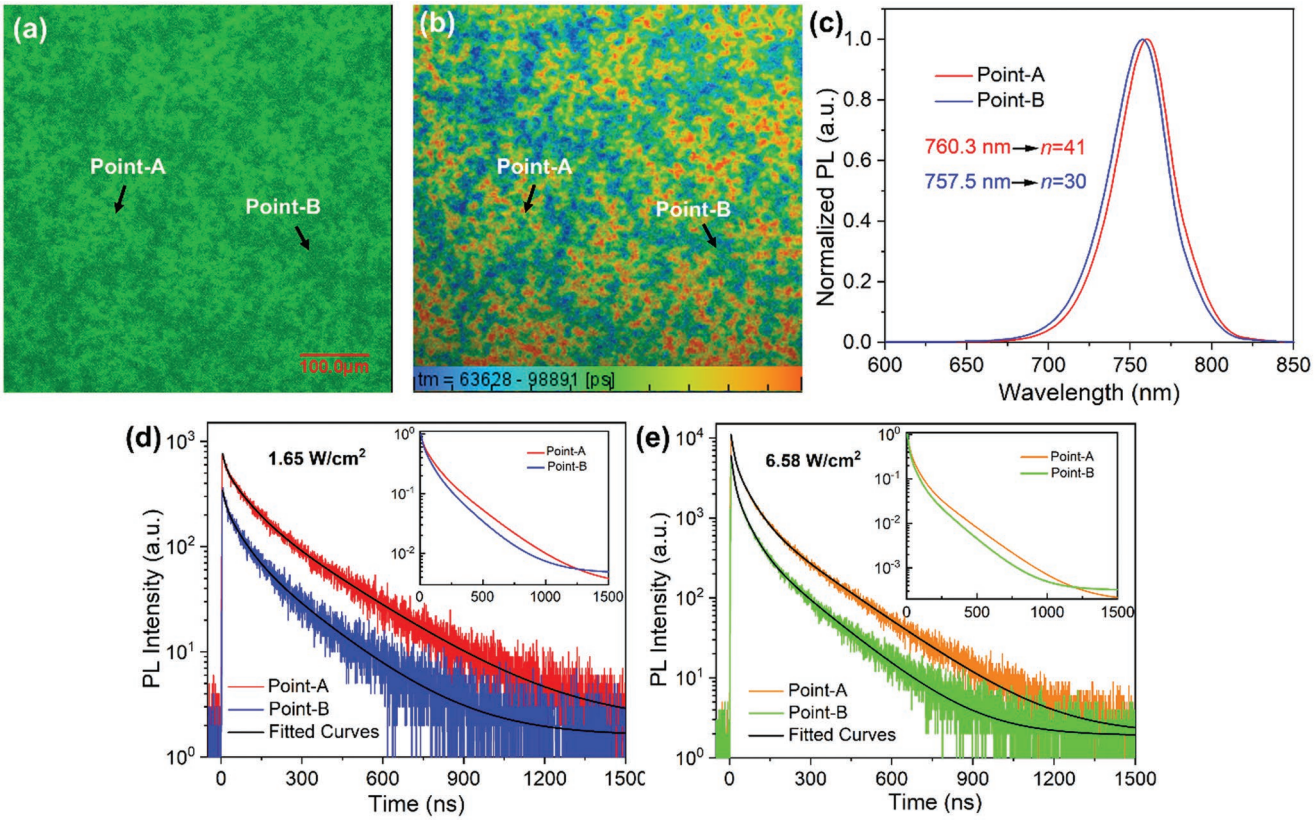

Figure 3. a) The PL intensity and b) the corresponding amplitude weighted average PL lifetime (τ_m) images of the hot-drop-cast $BA_2MA_{n-1}Pb_nI_{3n+1}$ ($\langle n \rangle = 5$) quasi-2D perovskite films; c) PL spectra collected from point-A (dendritic region) and point-B (nondendritic region); time-resolved PL decay profiles of point-A and point-B under d) low (1.65 W cm^{-2}) and e) high (6.58 W cm^{-2}) excitation intensity. (Excitation laser: 420 nm, 1.0 MHz.) The insets in (d) and (e) plot the intensity normalized best fits.

in Figure 3c. Despite the multiphase components of the quasi-2D perovskite film, both spectra collected from the front surface of the film are dominated by emission peaks assigned to large-*n* RPPs. This is largely due to the distribution of the large-*n* RPPs phase on the front side and the inter-phase charge carriers funneling from small-*n* to large-*n* RPPs before radiative recombination, according to our previous studies.[12] The average slab thickness (*n*) of RPPs responsible for the PL emission peak can be estimated using the following empirical Equation (3)[15]

$$E_x \approx \frac{1240}{\lambda_{PL}}(\text{eV}) = 1.623\,(\text{eV}) + \frac{1}{0.063\cdot n^2 + 0.458\cdot n + 0.811}(\text{eV}) \quad (3)$$

In this equation, E_x is the excitonic gap of RPPs and λ_{PL} is the PL peak position (nm). The numerical best matching *n* value (integer) obtained for RPPs from the dendritic and non-dendritic regions is about 30 and 40, respectively, indicating that the thickness of large-*n* RPPs in the front surface of dendrites is larger than in the nondendritic (pits) film area.

Figure 3d,e shows the PL decay profiles collected from the representative points A and B under low (1.65 W cm^{-2}) and high (6.58 W cm^{-2}) excitation intensity, respectively. All decay profiles were parameterized with a three-exponential decay function (Equation (1a)), giving the fitting values listed in **Table 1**. Under low excitation intensity (Figure 3d), the average PL lifetime (τ_m) of the perovskite film in the dendrite region (122 ± 3 ns) is larger than that of the nondendritic film area (94 ± 3 ns), which is consistent with the overall faster decay of the latter, shown by the normalized fits presented in the figure inset. Because the RPPs with larger slab thickness possess a longer average PL lifetime,[24] this result implies that perovskite components in the dendritic region have a larger average 2D-slab thickness compared to the nondendritic region. As mentioned before, PL collected for TRPL analysis is mainly from the large-*n* (*n* = L) RPPs phase layer in the front surface. When the excitation intensity increases to 6.58 W cm^{-2}, the average PL lifetimes from both regions are decreased to 45.7 ± 0.3 and 36.1 ± 0.2 ns, respectively, accompanied by an increase in the contribution of the faster decay component (A_1). This observation can be explained by the saturation of excited states in the large-*n* RPPs phase under high excitation intensity,[25] leading to the enhanced emission from carrier recombination in the medium-*n* RPPs which would otherwise undergo energy transfer to the large-*n* RPPs under low excitation intensity conditions. Since medium-*n* RPPs generally exhibit faster emission decay than large-*n* RPPs, the relatively larger A_1 for point-B (54.2%, nondendritic) compared to point-A (48.6%, dendritic) may be attributed to the closer distance of the medium-*n* RPPs phase layer toward the front surface of the perovskite film owing to the existence of sunken pits in the nondendritic region, that facilitates their photoexcitation and the PL emission. In summary, there are more large-*n* RPPs with larger average 2D slab thickness distributed in the dendritic film regions compared to the nondendritic areas, leading to a longer charge carrier lifetime. We expect that this would enhance carrier transport to the film surfaces, and thus generate a better photovoltaic performance in Brownian tree-shaped dendrites compared with other regions in the films.

Table 1. Fitting parameters for the decay profiles of point-A and B based on Equation (1).

		A_1	τ_1 [ns]	A_2	τ_2 [ns]	A_3	τ_3 [ns]	τ_m [ns]
1.65 W cm^{-2}	Point-A	24.5%	11.4 ± 0.6	41.7%	75 ± 3	33.8%	259 ± 6	122 ± 3
	Point-B	25.2%	11.1 ± 0.8	43.7%	60 ± 3	31.1%	210 ± 5	94 ± 3
6.58 W cm^{-2}	Point-A	48.6%	10.3 ± 0.1	40.0%	49.0 ± 0.2	11.4%	185 ± 1	45.7 ± 0.3
	Point-B	54.2%	9.8 ± 0.1	36.0%	42.6 ± 0.3	9.8%	158 ± 1	36.1 ± 0.2

To further consolidate the hypothesized formation mechanism of pits and dendrites in the quasi-2D perovskite films, GIWAXS characterization of $BA_2MA_{n-1}Pb_nI_{3n+1}$ (<*n*> = 5) quasi-2D perovskite films prepared without (w/o) and with MACl doping was carried out to examine differences in their structure and composition. **Figure 4**a shows the 2D GIWAXS scattering patterns of the as-prepared (fresh) $BA_2MA_{n-1}Pb_nI_{3n+1}$ (<*n*> = 5) quasi-2D perovskite film (w/o MACl) with the discrete Bragg diffraction spots indexed according to literature.[1b,11c] The appearance of strong and discrete ($1\bar{1}1$) and (202) diffraction spots along the out-of-plane (vertical) direction is an indication that 2D RPPs slabs are aligned perpendicular to the substrate.[11a] However, most of these spots spread out azimuthally, especially along $|q_r| \approx 1$ and 2 Å^{-1}, indicating the orientation of 2D RPPs within the un-doped quasi-2D perovskite film is mostly distributed orthogonally with a small portion randomly oriented. For the fresh quasi-2D perovskite film prepared with MACl doping, the GIWAXS image (Figure 4b) features similar scattering patterns as the nondoped film, with all the spots becoming more compact and the scattering rings at $|q_r| \approx 1$ and 2 Å^{-1} missing. The strong out-of-plane scattering peaks and the reduced contribution from the scattering ring is clear evidence that the 2D RPPs slabs are collectively aligned orthogonal to the substrate within the MACl-doped film. Based on the GIWAXS characterization of the MACl-doped quasi-2D perovskite aged in a nitrogen atmosphere for 1 month (Figure 4c), it was found that the alignment of 2D RPPs slabs perpendicular to the substrate is further enhanced. Figure 4d,e plots the sector integrated diffraction intensity profiles along the in-plane (horizontal) and the out-of-plane (vertical) directions. All the diffraction peaks are broader than the peaks from the 3D $MAPbI_3$ perovskite (Figure S6a,b, Supporting Information), which is not surprising given the multiphase nature of quasi-2D perovskite films composed of 2D RPPs with various thicknesses (*n*). The (0*k*0) and (02*k*0) peaks represent the X-ray diffraction based on the crystalline plane along the horizontal direction. The increased intensity of these peaks for the MACl-doped film indicates enhanced coordination between the adjacent RPPs slabs, or crystallinity. Aging of the MACl-doped film leads to further enhancement in crystallinity, as shown by the increase of peak intensity in Figure 4d.

Further insight into the size of RPPs can be gained by closer analysis of the peak shapes. In the out-of-plane direction, the ($1\bar{1}1$) peak can be regarded as the diffraction assembly from vertically aligned RPPs with various thicknesses. For individual 2D $BA_2MA_{n-1}Pb_nI_{3n+1}$ RPPs, the *q* value of the ($1\bar{1}1$) peak decreases with the increase of slab thickness *n*, i.e., decreasing from $\left|q_{(1\bar{1}1)}\right| = 1.006$ Å^{-1} for $n = 3$ to $\left|q_{(1\bar{1}1)}\right| = 0.995$ Å^{-1} for $n = \infty$.[12,26] The enlarged view of the ($1\bar{1}1$) diffraction peak in the inset

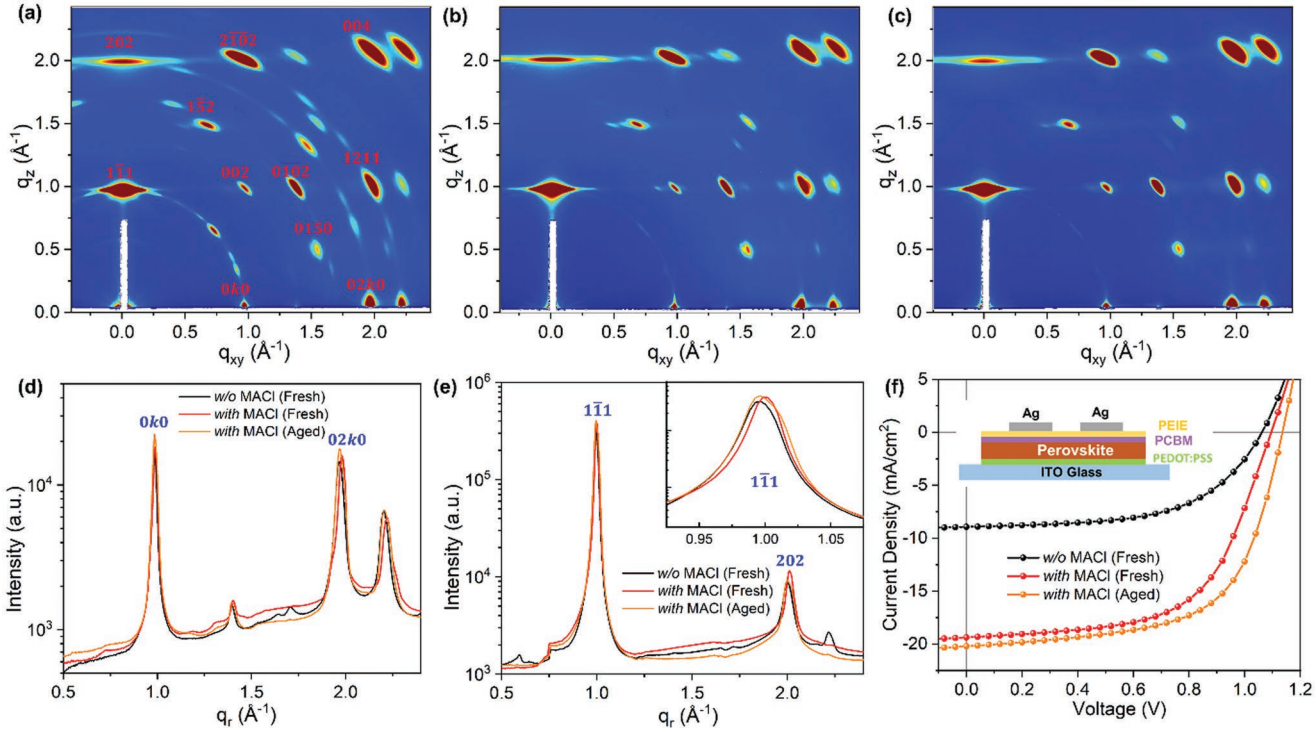

Figure 4. a) Indexed GIWAXS scattering patterns of the fresh $BA_2MA_{n-1}Pb_nI_{3n+1}$ (<*n*> = 5) quasi-2D perovskite film without MACl doping; GIWAXS scattering patterns of the b) fresh and c) aged $BA_2MA_{n-1}Pb_nI_{3n+1}$ (<*n*> = 5) quasi-2D perovskite films doped with MACl. The corresponding sector integrated intensity profiles along the d) in-plane (horizontal) and e) out-of-plane (vertical) directions; f) *J*–*V* curves of the 2D PSCs based on the three films (inset: the device structure).

(Figure 4e) shows the peak position for the fresh quasi-2D perovskite films prepared without and with MACl doping is peaked at 0.996 and 1.000 $Å^{-1}$, suggesting the average RPPs slab thickness for the fresh quasi-2D perovskite film decreases upon MACl doping. This is consistent with the observation that MACl doping facilitates the formation of small-*n* RPPs components in the STEM result.

2D PSCs based on the $BA_2MA_{n-1}Pb_nI_{3n+1}$ (<*n*> = 5) quasi-2D perovskite films prepared without (w/o) and with MACl doping were constructed to verify the effect of structural and compositional changes induced by MACl doping and the aging process on the photovoltaic performance. The structure of PSCs with the p-i-n configuration, which is composed of ITO (indium tin oxide) glass/PEDOT:PSS (poly(3,4-ethylenedioxy thiophene):polystyrene sulfonate)/quasi-2D perovskite/PEIE (polyethylenimine ethoxylated)/PCBM ([6,6]-phenyl-C61-butyric acid methyl ester)/Ag, is illustrated in the inset of Figure 4f. Figure 4f depicts the *J*–*V* curves of the champion PSCs based on the fresh un-doped (w/o MACl), fresh doped (with MACl), and aged doped (with MACl) quasi-2D perovskite films, respectively. The performance parameters including open-circuit voltage (V_{OC}), short-circuit current density (J_{SC}), fill factor (FF), and PCE of the champion PSCs and the average values from eight devices are summarized in **Table 2**. The highest PCE of the BA-based 2D PSCs increases from 5.39% to 12.64% upon 6 mol% MACl doping, and further to 14.19% after aging in the nitrogen atmosphere for 1 month, which is brought about by the increase of V_{OC}, J_{SC}, and FF. The significant increase in J_{SC} from 8.93 mA cm^{-2} for the fresh un-doped film to 19.38 and 20.21 mA cm^{-2} for the fresh and aged quasi-2D film with MACl doping is attributed to the ordered alignment of RPPs slabs with the perpendicular orientation that facilitates the charge transport and collection. The relatively small FF (55.86%) for the fresh un-doped quasi-2D perovskite film suggests a higher series resistance (R_s) that correlates with both the random orientation of RPPs and the low crystallinity of this film. The V_{OC} increase for MACl-doped quasi-2D film upon aging is explained by the increased average 2D RPPs slab thickness for the aged film, which possesses lower photo-voltage loss at the quasi-2D perovskite/PCBM interface. The enhanced crystallinity, improved vertical alignment, and increased average RPPs slab thickness are responsible for the J_{SC} and thus the PCE enhancement of the PSCs based on MACl-doped quasi-2D perovskite film upon aging.

Table 2. Summary of photovoltaic parameters of 2D PSCs based on the fresh and aged $BA_2MA_{n-1}Pb_nI_{3n+1}$ (<*n*> = 5) quasi-2D perovskite films without (w/o) and with MACl doping.

		V_{OC} [V]	J_{SC} [mA cm^{-2}]	FF [%]	PCE [%]
w/o MACl (Fresh)	Champion	1.08	−8.93	55.86	5.39
	Average	1.07 ± 0.01	−8.8 ± 0.3	54 ± 2	4.7 ± 0.4
with MACl (Fresh)	Champion	1.10	−19.38	60.40	12.64
	Average	1.09 ± 0.01	−18.9 ± 0.4	59.1 ± 2.2	12.1 ± 0.4
with MACl (Aged)	Champion	1.12	−20.21	62.71	14.19
	Average	1.12 ± 0.01	−19.7 ± 0.3	63 ± 1	13.7 ± 0.3

During these experiments, we also noticed that 2D PSCs based on the aged quasi-2D perovskite films (MACl-doped) possess an even higher PCE, 14.2%, compared to the device based on fresh films. This significant performance enhancement of 2D PSCs suggests that the aging process under nitrogen should be an attractive strategy for constructing efficient 2D PSCs based on other quasi-2D perovskite films (beyond BA cations).

For the aged MACl-doped quasi-2D perovskite film, the $(1\bar{1}1)$ peak position shifted back to 0.997 $Å^{-1}$, indicating the average RPPs slab thickness of the film increases with age. We speculate the slow evaporation of BA ligands, at a much slower rate compared to the MA^+, is responsible for the conversion of small-*n* RPPs to large-*n* RPPs as well as an increase in the slab thickness of large-*n* RPPs during the prolonged aging period. As large-*n* RPPs demonstrate better charge carrier transport in photovoltaic applications, this synergistic compositional evolution and structural refinement of quasi-2D perovskite films during the aging process should be expected to benefit the photovoltaic performance of 2D PSCs.

To investigate the compositional and structural evolution principle of the quasi-2D perovskite films featured by Brownian tree-shaped dendrites, TA spectroscopy was conducted to characterize the photophysical dynamics of the films upon aging. The 2D pseudocolor plots of the TA spectra ($m\Delta$OD: pump-induced absorbance change) for the fresh and aged MACl-doped $BA_2MA_{n-1}Pb_nI_{3n+1}$ ($<n> = 5$) quasi-2D perovskite films are presented in **Figure 5**a,b. The spectra were collected following 525 nm pulsed laser excitation (96 kHz, 1.6 μJ cm^{-2}) under the back-side (glass) excitation (transmitted probe detection) mode. Both spectra feature strong ground-state bleaching (GB) peaks assigned to the small-*n* ($n = 3, 4, 5$) RPPs phases at early pump-probe delays (0–100 ps). The GB peaks of large-*n* ($n = L$) RPPs at the long-wavelength region gradually emerge and dominate the spectra at longer delay times, accompanied by the diminishment of the small-*n* peaks. The 2D pseudocolor TA spectrum of the fresh un-doped quasi-2D perovskite film is presented in Figure S7a in the Supporting Information, showing similar features compared to the MACl-doped films. Figure 5c plots the TA spectra of the fresh and aged films as a function of probe wavelength at selected pump-probe delay times (0.5 and 5000 ps). The GB peak positions for $n = 3, 4, 5$ RPPs from both films are around 606, 643, and 670 nm, consistent with the literature reports.[25,27] The GB peaks of large-*n* ($n = L$) RPPs redshift with increasing pump-probe delay time from 0.5 to 5000 ps, indicative of hot-carrier cooling in both films. The final GB peak position for large-*n* RPPs in the aged film is redshifted relative to the fresh film (739 nm vs 733 nm), further confirms that the average thickness of RPPs slabs within the quasi-2D perovskite films increase upon aging. For comparison, the TA spectrum of the un-doped films as a function of probe wavelength recorded at 0.5 ps pump-probe delay is shown in Figure S7b in the Supporting Information. The prominent difference with the doped films lies in the overall compositional ratio of the large-*n* RPPs, the lower GB peak ratio of $I(n = L)/I(n = 3)$ (≈0.42) for the MACl-doped quasi-2D films compared to that of nondoped films (≈0.67). This is consistent with the fact that MACl doping

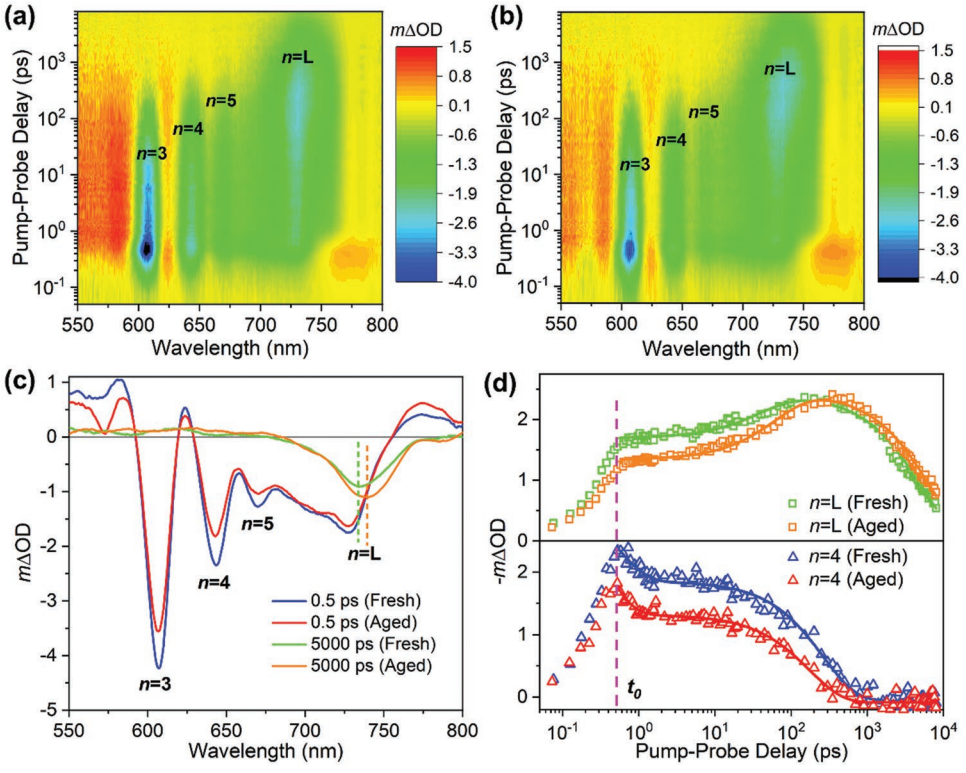

Figure 5. Pseudo-color 2D plots of TA spectra ($m\Delta$OD) of the a) fresh and b) aged $BA_2MA_{n-1}Pb_nI_{3n+1}$ ($<n> = 5$) quasi-2D perovskite films doped with MACl; c) TA spectra as a function of probe wavelength recorded at various pump-probe delays. d) The decay profiles of the $-m\Delta$OD signal for the GB peaks of small-*n* ($n = 4$) and large-*n* ($n = L$) RPPs.

facilitates the escape of MA cations from the films to form pits in the nondendritic areas and is also aligned with our previous finding that MACl can facilitate the crystallization of small-*n* RPPs.[15]

The exciton dynamics within the fresh and aged quasi-2D perovskite films are obtained by the temporal decay of each GB peak. The decay profiles of the $-m\Delta OD$ signal for the representative GB peaks from small-*n* ($n = 4$) and large-*n* ($n = L$) RPPs are plotted in the lower and upper panel of Figure 5d. Following excitation, the conduction band (CB) of $n = 4$ for both films reaches the maximum values at the same time, $t_0 = 0.5$ ps. Thereafter, the GB signal of $n = 4$ RPPs decays rapidly while that of $n = L$ RPPs undergoes a corresponding rise and decline in intensity, which can be regarded as a sign of the inter-phase exciton transfer from small-*n* to large-*n* RPPs, followed by the eventual decay of large-*n* excited state.[28] All decay profiles can be well-fit by the following two-exponential function (Equation (4))

$$I_{-m\Delta OD}(t) = A_1 \exp\left(-\frac{t-t_0}{\tau_1}\right) + A_2 \exp\left(-\frac{t-t_0}{\tau_2}\right) \quad (4)$$

In this equation, $t_0 =$ 0.5 ps, τ_1, A_1, τ_2, A_2 are the recovered lifetimes and corresponding amplitudes, which are all summarized in **Table 3**. The fast decay component (τ_1) for $n = 4$ RPPs reflects the dominance of the nonradiative exciton–exciton annihilation process.[29] The slow decay in $n = 4$ RPPs is representative of the intrinsic radiative exciton recombination and the exciton transfer to the large-*n* RPPs. The smaller τ_2 for the aged quasi-2D perovskite film (180 ± 12 ps) compared to that of the fresh film (270 ± 14 ps) implies more efficient exciton transfer occurring in the small-*n* RPPs. For the decay profiles of the large-*n* GB signals, component (τ_1) shows a negative amplitude that is attributed to the accumulation of excitons transferred from the small-*n* RPPs. The negative amplitude A_1% for the fresh film (23.1%) increases to 31.9% for the aged film, suggesting the efficiency of exciton transfer (funneling) from the small-*n* to large-*n* RPPs is enhanced in quasi-2D perovskite films upon aging. The longer decay time (τ_2) for the large-*n* RPPs of the aged quasi-2D film (6200 ± 120 ps) is a consequence of a longer free-carrier lifetime in this film, which is attributed to the increased averaged thickness of the component RPPs. All these factors are beneficial for the photovoltaic performance of 2D PSCs in terms of the efficient exciton funneling and the effective collection of long-lifetime free carriers by electrodes, which is consistent with the performance of 2D PSCs demonstrated in Figure 4f.

Table 3. Fitting parameters for decay profiles of GB peaks ($-m\Delta OD$) of the $n = 4$ and $n = L$ RPPs from the fresh and aged $BA_2MA_{n-1}Pb_nI_{3n+1}$ ($<n> = 5$) quasi-2D perovskite films.

		A_1	τ_1 [ps]	A_2	τ_2 [ps]
$n = 4$	Fresh	0.54 ± 0.06	0.47 ± 0.09	1.91 ± 0.02	270 ± 14
	Aged	0.45 ± 0.06	0.28 ± 0.07	1.40 ± 0.02	180 ± 12
$n = L$	Fresh	−0.69 ± 0.02	41 ± 4	2.30 ± 0.02	4830 ± 95
	Aged	−1.09 ± 0.02	66 ± 4	2.33 ± 0.02	6200 ± 120

Based on all the results above, the landscape of the BA-based quasi-2D perovskite films can be summarized as follows. According to the SEM and AFM images, the nondendritic film area comprises perovskite grains centered with pits while the perovskite grains with relatively smooth surfaces assemble into the dendrites with lateral size of hundreds of micrometers. STEM and PL characterization indicates that the perovskite grains from the dendritic regions are dominated by the large-*n* 2D RPPs while the grains from the nondendritic area are rich in small-*n* 2D RPPs. The computer simulation and the AFM results illustrate that the individual perovskite grains (≈1–2 µm) are the building blocks of the Brownian tree-shaped dendrites. These randomly branched dendrites formed in the MACl-doped quasi-2D perovskite are comparable to the radial clusters observed in the 3D $MAPbI_3$ perovskite films, which are caused by the facet crystal growth from a central nucleation site during film formation. Therefore, we speculate that MA-rich intermediate phase domains are formed after the dropping of precursor solution onto the hot substrate. Instead of facet stacking of these domains set up in 3D perovskite systems, owing to the crystallization perturbation induced by the BA spacer cations within them, they tend to connect by random collisions during their Brownian motion, which is guided by the DLA principle, to form the Brownian tree-shaped dendrites. As illustrated in **Figure 6**, the initial crystallization of these intermediate dendrites inevitably squeezes the majority of BA^+ and MACl into the remaining solution onto the other film areas, which gradually crystallizes into a uniform assembly of the BA-rich intermediate phase domains. After complete evaporation of DMF solvent, the MA-rich phase domain patterns convert into Brownian tree-shaped dendrites of perovskites dominated by large-*n* RPPs, while the BA-rich intermediate phase regions turn into the nondendritic film areas composed of small-*n* RPPs-dominated perovskite grains that contain numerous pits, which are generated by the MACl evaporation-induced film surface collapse. As the dendrites are not able to be formed in quasi-2D perovskite without MACl doping, we propose the role of MACl doping is mainly to facilitate the separation of MA- and BA-rich intermediate phase domains. As revealed by the GIWAXS and TA studies combined with the performance characterization of the constructed 2D PSCs, the formation of these dendrites in quasi-2D perovskite films upon MACl doping is

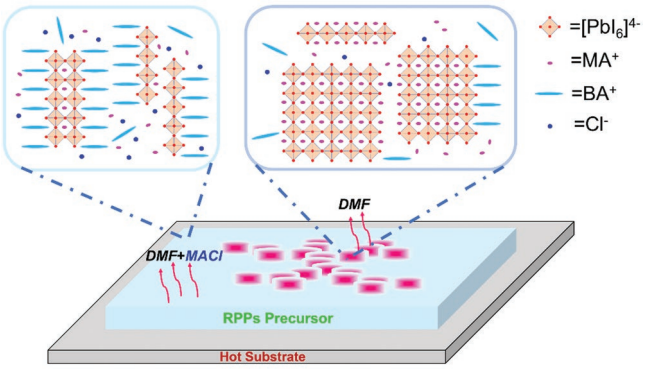

Figure 6. Schematic illustration for the growth of the MACl-doped $BA_2MA_{n-1}Pb_nI_{3n+1}$ quasi-2D perovskite films governed by the diffusion-limited aggregation (DLA) of MA-rich phase domains.

accompanied by the improved organization and crystallinity of the component 2D RPPs, thus substantially benefitting the photovoltaic performance of 2D PSCs. Aging the MACl-doped quasi-2D perovskite films in the nitrogen atmosphere causes the gradual evaporation (escape) of BA spacers, leading to the compositional and structural refinement of the films that further assists the optimization of 2D PSCs.

3. Conclusions

The landscape of the quasi-2D RPP films featuring Brownian tree-shaped dendrites was systematically characterized in this work using optical, electronic, atomic force, and fluorescence microscopies, as well as GIWAXS and TA spectroscopies. These investigations reveal that the dendrites are assembled comprising large-*n* RPPs dominated perovskite grains with smooth surfaces, while the nondendritic film area is composed of the small-*n* RPPs dominated perovskite grains and associated with film surface indentations (or pits) caused by the evaporation of MACl. We propose that these dendrites are grown by the DLA of the MA-rich intermediate phase domains that initially crystallized from the precursor, leading to the enrichment of butylammonium (BA) spacers and MACl in the residual solution that eventually convert into the small-*n* RPPs-dominated nondendritic film area full of MACl evaporation-induced pits. The formation of these dendrites in quasi-2D perovskite films upon MACl doping is accompanied by the improved organization and crystallinity of the component 2D RPPs, thus substantially benefitting the photovoltaic performance of 2D PSCs. Aging the MACl-doped quasi-2D perovskite films in a nitrogen atmosphere causes the gradual evaporation (escape) of BA spacers, leading to compositional and structural refinements of the film that are effective for further optimization of 2D PSCs.

In summary, this work provides an understanding of the formation mechanism of quasi-2D perovskite films by unveiling the origin of Brownian tree-shaped dendrites that generally appear in these films. The outcome of this research has implications for film structure and device engineering strategies that should prove advantageous for further improving the performance of optoelectronic devices based on quasi-2D RPP films.

4. Experimental Section

Preparation of Quasi-2D Perovskite Films: Lead iodide (PbI_2, Alfa Aesar, 230.7 mg), methylammonium iodide (MAI, Greatcell Solar, 63.6 mg), and *n*-butylammonium iodide (BAI, Greatcell Solar, 40.3 mg) were dissolved into 2 mL DMF (anhydrous DMF, Sigma-Aldrich) with magnetic stirring on a 70 °C hot plate for 1 h. After cooling down this solution to room temperature (RT), 2.0 mg methylammonium chloride (MACl, Greatcell Solar) was added followed by stirring at RT for 1 h to obtain a 0.25 M (concerning Pb^{2+}) precursor solution of $BA_2MA_{n-1}Pb_nI_{3n+1}$ ($\langle n\rangle$ = 5) perovskite doped with 6 mol% MACl. Pure-2D BA_2PbI_4 ($\langle n\rangle$ = 1) perovskite precursor was prepared by adding 230.7 mg PbI_2 and 201.1 mg BAI into 2 mL DMF and stirring on a 70 °C hot plate for 1 h. 2.0 mg MACl was added to this solution after cooling down to RT followed by stirring for another 1 h to obtain the 6 mol% MACl-doped BA_2PbI_4 ($\langle n\rangle$ = 1) perovskite precursor (0.25 M). By replacing the BAI (40.3 mg) with 4-fluoro-phenethylammonium iodide (f-PEAI, Greatcell Solar, 53.4 mg) and adding 2.7 mg of ammonium chloride (NH_4Cl) instead for MACl, 2 mL 0.25 M f-$PEA_2MA_{n-1}Pb_nI_{3n+1}$ ($\langle n\rangle$ = 5) quasi-2D perovskite precursor (doped with 10 mol% NH_4Cl) was obtained. A 0.8 M MACl-doped $BA_2MA_{n-1}Pb_nI_{3n+1}$ ($\langle n\rangle$ = 5) precursor solution was prepared by a proportional increase in the amount of each component (with the ratio of 8/3), with 738.1 mg PbI_2, 203.5 mg MAI, 128.6 mg BAI dissolved in 2 mL DMF and 6.5 mg MACl added. The $BA_2MA_{n-1}Pb_nI_{3n+1}$ ($\langle n\rangle$ = 5) or f-$PEA_2MA_{n-1}Pb_nI_{3n+1}$ ($\langle n\rangle$ = 5) quasi-2D perovskite films were deposited from the corresponding precursor solution (0.25 M) by the one-step drop-casting method. 5 µL precursor was dropped onto the center of a UV-ozone treated clear glass substrate (2.5 cm × 2.5 cm), which was placed on a 60 °C hot plate, and spread out to form a circular film after the evaporation of DMF. The film was then transferred to a 100 °C hot plate for 2 min of annealing. For films prepared by the hot-spin-coating method, 50 µL of 6 mol% MACl-doped $BA_2MA_{n-1}Pb_nI_{3n+1}$ ($\langle n\rangle$ = 5) (0.8 M) was dropped onto a clear glass substrate, which was preheated to 100 °C on a hot plate and immediately transferred to a vacuum chuck of a spin-coater, and spin-coated at 3000 rpm for 35 s. After the subsequential annealing at 100 °C for 2 min, hot-spin-cast quasi-2D $BA_2MA_{n-1}Pb_nI_{3n+1}$ ($\langle n\rangle$ = 5) films were prepared. The reference $MAPbI_3$ (3D) films were coated from the precursor solution in DMF onto the bare glass substrates by a slot-die method reported in previous work.[14c] The MACl-doped $BA_2MA_{n-1}Pb_nI_{3n+1}$ ($\langle n\rangle$ = 5) quasi-2D perovskite films were placed in a nitrogen-filled glove box and kept for 1 month to complete the aging process. All quasi-2D perovskite films reported in this manuscript were, unless otherwise specified, the as-prepared (fresh) film samples.

Fabrication and Characterization of 2D PSCs: Prepatterned ITO glass plates (5 ohms per square) were sequentially cleaned by ultrasound sonication in detergent, deionized water, acetone, isopropyl alcohol for 5 min, successively. After 15 min of UV ozone treatment, a PEDOT:PSS (Agfa Clevious ALP 4083) hole transporting layer (HTL) was added by spin coating at 5000 rpm followed by 15 min of annealing at 140 °C. $BA_2MA_{n-1}Pb_nI_{3n+1}$ ($\langle n\rangle$ = 5) quasi-2D perovskite films without and with MACl doping were deposited by the one-step hot-drop-casting method, with the latter optionally aged for 1 month in the N_2-filled glove box. PSCs with the structure of ITO/PEDOT:PSS/quasi-2D perovskite/PCBM/PEIE/Ag and active area of 0.1 cm^2 were fabricated according to the procedure detailed in previous work.[15] Current density–voltage (*J*–*V*) curves of 2D PSCs were measured using a Keithley 2400 Source Meter with the reverse scan mode (rate: 30 mV s^{-1}) under standard solar illumination (AM 1.5G, 100 mW cm^{-2}).

Optical and AFM Characterization: The optical transmission imaging of the quasi-2D perovskite films on glass substrates was performed by illuminating the films from the top side using a halogen lamp-generated white light and collecting the transmitted signals from the bottom side by a high-resolution digital camera (Nikon). Both AFM 2D morphology and KPFM characterizations of quasi-2D perovskite films were carried out by AFM (Asylum Research Cypher ES) using conductive probes in the tapping mode.

SEM and STEM Characterization: An SEM (FEI Teneo) was used to obtain the top-view SEM images of the hot-drop-cast $BA_2MA_{n-1}Pb_nI_{3n+1}$ ($\langle n\rangle$ = 5) quasi-2D perovskite films. The lamella sample of the $BA_2MA_{n-1}Pb_nI_{3n+1}$ ($\langle n\rangle$ = 5) quasi-2D perovskite film for the STEM measurement was prepared using an FEI Nanolab 200 FIB system at the Ian Holmes Imaging Center, Bio21 Institute. Pt (platinum) protection layers were first deposited using e-beam and then using i-beam on the thin carbon layer-coated quasi-2D perovskite film surface as the etching mask. After ion beam etching with 30 keV Ga FIB, the lamella was lifted off and transferred to the copper grid using an internal micro-manipulator. Several cycles of low keV gentle milling were applied to finally obtain a cross-sectional lamella of glass/quasi-2D perovskite/carbon/Pt with ≈100 nm thickness. The HAADF STEM images of the prepared lamella were obtained by an FEI Tecnai TF20 high-resolution TEM under the HAADF detection mode.

GIWAXS Characterization: GIWAXS measurements of the fresh and aged $BA_2MA_{n-1}Pb_nI_{3n+1}$ ($\langle n\rangle$ = 5) quasi-2D perovskite films without and with MACl doping were performed at the Australian Synchrotron using the

SAXS/WAXS beamline with a photon energy fixed at 15 keV and an in-vacuum (< 1 × 10–5 mbar) Pilatus 2M CCD as the detector. The incidence light angle was 0.2° and the sample to detector distance was set as 600 mm.

PL and TRPL Microspectroscopy: The PL and the TRPL of the drop-cast $BA_2MA_{n-1}Pb_nI_{3n+1}$ (<*n*> = 5) quasi-2D perovskite films were measured using a scanning confocal microscope (Olympus, IX71/FV300), equipped with either a fluorescence spectrometer or a TCSPC setup. The 420 nm excitation beam was the frequency-doubled output of a mode-locked and cavity dumped Ti:Sapphire laser (Coherent Mira900f/APE PulseSwitch, 100 fs FWHM) which was focused on the front surface of films through a 10 × objective lens, with the laser spot size estimated to be 2.0×10^{-8} cm^2. The PL emission collected by the same objective lens was filtered by an appropriate highpass filter and detected confocally by a fluorescence spectrometer (Ocean Optics, Maya) for obtaining the PL spectra, or by a single photon counting photomultiplier (Becker & Hickl, PMC-100-1) for the TRPL measurements. TRPL profiles were recorded using a commercial photon counting system (SPC150 card, Becker & Hickl, Germany) with an instrument response function of ≈200 ps. PL and TRPL images were generated by scanning the 420 nm excitation laser over the front surface of drop-cast quasi-2D perovskite films in the range of some hundreds of microns. The laser used for PL and TRPL measurements had a pulse repetition rate of 1.0 MHz and was used with intensities of 1.65 W cm^{-2} (low intensity) and 6.58 W cm^{-2} (high intensity).

TA Spectroscopy: Femtosecond pump-probe TA measurements for the fresh and aged $BA_2MA_{n-1}Pb_nI_{3n+1}$ (<*n*> = 5) quasi-2D perovskite films doped with MACl were performed using a TA spectrometer at room temperature. The 800 nm pulsed output (96 kHz, 60 fs FWHM) generated by a high repetition rate amplifier (Coherent RegA 9050) was split to generate the pump (525 nm) beam through a tunable optical parametric amplifier (Coherent OPA 9450) and the probe (visible/near-IR white light) beam using a 3 mm thick sapphire window (CASTECH), respectively. Pump and probe pulses were focused by an off-axis parabolic reflector to overlap at the surface of the film sample with a pump spot size of ≈200 µm, giving an excitation fluence of 1.6 µJ cm^{-2}. Pump-induced absorption changes (ΔOD) were measured by comparing transmitted probe pulses with and without pump pulses modulated by a synchronized mechanical chopper in the path of the pump beam. The time-resolved transient absorption spectra were recorded using a high-speed fiber-optic spectrometer (Ultrafast Systems). The TA spectra of the quasi-2D perovskite film were collected under the back-side (glass) excitation (transmitted probe detection) mode.

Supporting Information

Supporting Information is available from the Wiley Online Library or from the author.

Acknowledgements

Funding support from the ARC Centre of Excellence in Exciton Science (CE170100026) is acknowledged. T.A.S., M.G., and D.A. acknowledge support from the Australian Centre for Advanced Photovoltaics (ACAP) program funded by the Australian Government through the Australian Renewable Energy Agency (ARENA), and the Industrial Innovation Program of CSIRO Manufacturing. GIWAXs measurements were undertaken on the SAXS/WAXS beamline at the Australian Synchrotron facilities, part of ANSTO.

Open access publishing facilitated by The University of Melbourne, as part of the Wiley – The University of Melbourne agreement via the Council of Australian University Librarians.

Conflict of Interest

The authors declare no conflict of interest.

Data Availability Statement

The data that support the findings of this study are available in the supplementary material of this article.

Keywords

dendrites, diffusion-limited aggregation, exciton transfer, film structure, perovskite solar cells, quasi-2D Ruddlesden–Popper perovskites

Received: November 15, 2021
Revised: January 11, 2022
Published online: February 6, 2022

[1] a) D. H. Cao, C. C. Stoumpos, O. K. Farha, J. T. Hupp, M. G. Kanatzidis, *J. Am. Chem. Soc.* **2015**, *137*, 7843; b) H. Tsai, W. Nie, J. C. Blancon, C. C. Stoumpos, R. Asadpour, B. Harutyunyan, A. J. Neukirch, R. Verduzco, J. J. Crochet, S. Tretiak, L. Pedesseau, J. Even, M. A. Alam, G. Gupta, J. Lou, P. M. Ajayan, M. J. Bedzyk, M. G. Kanatzidis, *Nature* **2016**, *536*, 312.

[2] a) C. C. Stoumpos, D. H. Cao, D. J. Clark, J. Young, J. M. Rondinelli, J. I. Jang, J. T. Hupp, M. G. Kanatzidis, *Chem. Mater.* **2016**, *28*, 2852; b) H. H. Fang, J. Yang, S. Adjokatse, E. Tekelenburg, M. E. Kamminga, H. Duim, J. Ye, G. R. Blake, J. Even, M. A. Loi, *Adv. Funct. Mater.* **2019**, *30*, 1907979.

[3] a) Y. Yang, C. Liu, A. Mahata, M. Li, C. Roldán-Carmona, Y. Ding, Z. Arain, W. Xu, Y. Yang, P. A. Schouwink, A. Züttel, F. De Angelis, S. Dai, M. K. Nazeeruddin, *Energy Environ. Sci.* **2020**, *13*, 3093; b) C. Zuo, A. D. Scully, D. Vak, W. Tan, X. Jiao, C. R. McNeill, D. Angmo, L. Ding, M. Gao, *Adv. Energy Mater.* **2019**, *9*, 1803258; c) H. Lai, B. Kan, T. Liu, N. Zheng, Z. Xie, T. Zhou, X. Wan, X. Zhang, Y. Liu, Y. Chen, *J. Am. Chem. Soc.* **2018**, *140*, 11639; d) H. Lai, D. Lu, Z. Xu, N. Zheng, Z. Xie, Y. Liu, *Adv. Mater.* **2020**, *32*, 2001470.

[4] X. Xiao, J. Dai, Y. Fang, J. Zhao, X. Zheng, S. Tang, P. N. Rudd, X. C. Zeng, J. Huang, *ACS Energy Lett.* **2018**, *3*, 684.

[5] M. D. Smith, B. A. Connor, H. I. Karunadasa, *Chem. Rev.* **2019**, *119*, 3104.

[6] a) Y. Liu, H. Ye, Y. Zhang, K. Zhao, Z. Yang, Y. Yuan, H. Wu, G. Zhao, Z. Yang, J. Tang, Z. Xu, S. Liu, *Matter* **2019**, *1*, 465; b) K. Wang, C. Wu, D. Yang, Y. Jiang, S. Priya, *ACS Nano* **2018**, *12*, 4919; c) F. Thouin, D. A. Valverde-Chavez, C. Quarti, D. Cortecchia, I. Bargigia, D. Beljonne, A. Petrozza, C. Silva, A. R. Srimath Kandada, *Nat. Mater.* **2019**, *18*, 349.

[7] A. H. Proppe, M. H. Elkins, O. Voznyy, R. D. Pensack, F. Zapata, L. V. Besteiro, L. N. Quan, R. Quintero-Bermudez, P. Todorovic, S. O. Kelley, A. O. Govorov, S. K. Gray, I. Infante, E. H. Sargent, G. D. Scholes, *J. Phys. Chem. Lett.* **2019**, *10*, 419.

[8] a) J. Hu, I. W. H. Oswald, S. J. Stuard, M. M. Nahid, N. Zhou, O. F. Williams, Z. Guo, L. Yan, H. Hu, Z. Chen, X. Xiao, Y. Lin, Z. Yang, J. Huang, A. M. Moran, H. Ade, J. R. Neilson, W. You, *Nat. Commun.* **2019**, *10*, 1276; b) F. Zhang, D. H. Kim, H. Lu, J. S. Park, B. W. Larson, J. Hu, L. Gao, C. Xiao, O. G. Reid, X. Chen, Q. Zhao, P. F. Ndione, J. J. Berry, W. You, A. Walsh, M. C. Beard, K. Zhu, *J. Am. Chem. Soc.* **2019**, *141*, 5972.

[9] C. M. M. Soe, W. Nie, C. C. Stoumpos, H. Tsai, J.-C. Blancon, F. Liu, J. Even, T. J. Marks, A. D. Mohite, M. G. Kanatzidis, *Adv. Energy Mater.* **2018**, *8*, 1700979.

[10] a) N. Zhou, Y. Zhang, Z. Huang, Z. Guo, C. Zhu, J. He, Q. Chen, W. Sun, H. Zhou, *ACS Nano* **2021**, *15*, 8350; b) Y. Yang, C. Liu, H. Kanda, Y. Ding, H. Huang, H. Chen, B. Ding, Y. Liang, X. Liu, M. Cai, P. J. Dyson, S. Dai, M. K. Nazeeruddin, *Adv. Funct. Mater.* **2021**, *31*, 2104868.

[11] a) Z. Wang, Q. Wei, X. Liu, L. Liu, X. Tang, J. Guo, S. Ren, G. Xing, D. Zhao, Y. Zheng, *Adv. Funct. Mater.* **2020**, *31*, 2008404; b) J. Liu, J. Leng, K. Wu, J. Zhang, S. Jin, *J. Am. Chem. Soc.* **2017**, *139*, 1432; c) Y. Lin, Y. Fang, J. Zhao, Y. Shao, S. J. Stuard, M. M. Nahid, H. Ade, Q. Wang, J. E. Shield, N. Zhou, A. M. Moran, J. Huang, *Nat. Commun.* **2019**, *10*, 1008.

[12] F. Zheng, C. R. Hall, D. Angmo, C. Zuo, S. Rubanov, Z. Wen, S. J. Bradley, X.-T. Hao, M. Gao, T. A. Smith, K. P. Ghiggino, *J. Mater. Chem. C* **2021**, *9*, 5362.

[13] Y. Xu, M. Wang, Y. Lei, Z. Ci, Z. Jin, *Adv. Energy Mater.* **2020**, *10*, 2002558.

[14] a) S. Sánchez, X. Hua, A. Günzler, E. Bermúdez-Ureña, D. Septiadi, M. Saliba, U. Steiner, *Cryst. Growth Des.* **2020**, *20*, 670; b) S. Sanchez, L. Pfeifer, N. Vlachopoulos, A. Hagfeldt, *Chem. Soc. Rev.* **2021**, *50*, 7108; c) D. Angmo, G. DeLuca, A. D. Scully, A. S. R. Chesman, A. Seeber, C. Zuo, D. Vak, U. Bach, M. Gao, *Cell Rep. Phys. Sci.* **2021**, *2*, 100293.

[15] F. Zheng, C. Zuo, M. Niu, C. Zhou, S. J. Bradley, C. R. Hall, W. Xu, X. Wen, X. Hao, M. Gao, T. A. Smith, K. P. Ghiggino, *ACS Appl. Mater. Interfaces* **2020**, *12*, 25980.

[16] a) T. A. Witten, L. M. Sander, *Phys. Rev. Lett.* **1981**, *47*, 1400; b) H. E. Stanley, P. Meakin, *Nature* **1988**, *335*, 405; c) H. Brune, C. Romainczyk, H. Roder, K. Kern, *Nature* **1994**, *369*, 469.

[17] A. Karperien, W. Rasband, Diffusion Limited Aggregate Models, https://imagej.nih.gov/ij/plugins/DLA.html (accessed: July 2021).

[18] J. Y. Ma, J. Ding, H. J. Yan, D. Wang, J. S. Hu, *ACS Appl. Mater. Interfaces* **2019**, *11*, 21627.

[19] J. Yang, S. Xiong, J. Song, H. Wu, Y. Zeng, L. Lu, K. Shen, T. Hao, Z. Ma, F. Liu, C. Duan, M. Fahlman, Q. Bao, *Adv. Energy Mater.* **2020**, *10*, 2000687.

[20] F. Zheng, W. Chen, T. Bu, K. P. Ghiggino, F. Huang, Y. Cheng, P. Tapping, T. W. Kee, B. Jia, X. Wen, *Adv. Energy Mater.* **2019**, *9*, 1901016.

[21] L. Cabana, B. Ballesteros, E. Batista, C. Magen, R. Arenal, J. Oro-Sole, R. Rurali, G. Tobias, *Adv. Mater.* **2014**, *26*, 2016.

[22] S. G. Motti, T. Crothers, R. Yang, Y. Cao, R. Li, M. B. Johnston, J. Wang, L. M. Herz, *Nano Lett.* **2019**, *19*, 3953.

[23] Y. Xu, J. Zhou, T. A. Smith, *Methods Appl. Fluoresc.* **2019**, *8*, 014006.

[24] a) L. N. Quan, M. Yuan, R. Comin, O. Voznyy, E. M. Beauregard, S. Hoogland, A. Buin, A. R. Kirmani, K. Zhao, A. Amassian, D. H. Kim, E. H. Sargent, *J. Am. Chem. Soc.* **2016**, *138*, 2649; b) C. M. Mauck, W. A. Tisdale, *Trends Chem.* **2019**, *1*, 380.

[25] G. Xing, B. Wu, X. Wu, M. Li, B. Du, Q. Wei, J. Guo, E. K. Yeow, T. C. Sum, W. Huang, *Nat. Commun.* **2017**, *8*, 14558.

[26] C. C. Stoumpos, C. M. M. Soe, H. Tsai, W. Nie, J.-C. Blancon, D. H. Cao, F. Liu, B. Traoré, C. Katan, J. Even, A. D. Mohite, M. G. Kanatzidis, *Chem* **2017**, *2*, 427.

[27] X. Wu, M. T. Trinh, D. Niesner, H. Zhu, Z. Norman, J. S. Owen, O. Yaffe, B. J. Kudisch, X. Y. Zhu, *J. Am. Chem. Soc.* **2015**, *137*, 2089.

[28] M. Yuan, L. N. Quan, R. Comin, G. Walters, R. Sabatini, O. Voznyy, S. Hoogland, Y. Zhao, E. M. Beauregard, P. Kanjanaboos, Z. Lu, D. H. Kim, E. H. Sargent, *Nat. Nanotechnol.* **2016**, *11*, 872.

[29] Z. Gan, X. Wen, C. Zhou, W. Chen, F. Zheng, S. Yang, J. A. Davis, P. C. Tapping, T. W. Kee, H. Zhang, B. Jia, *Adv. Opt. Mater.* **2019**, *7*, 1900971.